Received: 4 July 2023 | Accepted: 14 December 2023

DOI: 10.1002/maco.202313977

ARTICLE

Materials and Corrosion

An assessment of pitting corrosion in anodized aluminum alloys: It might not be what it seems

João Victor de Sousa Araujo[1] | Mariana Xavier Milagre[1] | Xiaorong Zhou[2] | Isolda Costa[1]

[1]Centro de Ciência e Tecnologia de Materiais, Instituto de Pesquisas Energéticas e Nucleares—IPEN/CNEN, São Paulo, Brasil

[2]School of Materials, Corrosion and Protection Centre, The University of Manchester, Manchester, UK

Correspondence
João Victor de Sousa Araujo, Materials Science and Technology Center, Nuclear and Energy Research Institute—IPEN/CNEN, Av. Prof. Lineu Prestes, 2242 São Paulo, Brazil.
Email: jvaraujo@usp.br

Funding information
Fundação de Amparo à Pesquisa do Estado de São Paulo (FAPESP), Grant/Award Numbers: 2019/18388-1, 2022/06935-0; Conselho Nacional de Desenvolvimento Científico e Tecnológico (CNPq), Grant/Award Number: 406871/2021-3

Abstract

In this study, special attention was given to the characterization of pits on the anodized aluminum alloy (Al–Zn–Mg–Cu) with an anodic aluminum oxide formed in tartaric sulfuric acid. Anodic polarization in 0.1 mol L^{-1} NaCl solution was used to initiate pitting corrosion in the anodized alloy. Pit characteristics, such as morphology and depth, were evaluated by using optical microscopy and optical profilometry, and scanning electron microscopy. The methodology adopted in this study revealed severe under-film pitting due to highly occluded conditions and showed that the extent of the under-film pitting is significantly greater than the size of pit mouth observed from the surface.

KEYWORDS

anodic polarization, image analysis, pit morphology, optical profilometer (OP), SEM (BSE-SE)

1 | INTRODUCTION

For passive metals, such as aluminum, the corrosion resistance properties are primarily due to the natural formation of an oxide film, a few nanometers thick, which isolates the metal from the medium.[1–5] The anodizing process consists of thickening this natural oxide film by applying an anodic potential or current to the metal surface in an electrolyte.[4] For Al alloys, this procedure leads to the formation of two layers depending on the composition of the anodizing bath: a barrier layer, which is thicker than the naturally formed oxide and more corrosion resistant, and a layer thicker than the barrier, which presents a structure of ordered pores, called a porous layer.[1,2,5,6] Therefore, understanding how corrosion propagates in anodized alloys and analyzing its extension and morphology are of great importance.[7–12]

The works from Takahashi et al.,[13,14] Zhou et al.,[15] Ren and Zuo,[16] and Moutarlier et al.[17] are the only ones in the literature that have investigated the pit corrosion characteristics of anodized aluminum alloys using polarization curves. However, the real extension of the corrosive attack associated with pitting on the anodized alloy was not addressed in any of these works.

Takahashi et al.[13,14] studied the corrosion behavior of Al with a high purity degree (99.99%) after cathodic polarization tests. The authors observed that only the central part of the pits remained open for the solution access and the periphery was covered with an anodic oxide film. The same was reported by Zuo et al.[15] when studying the influence of different sealing methods on pitting resistance of anodized aluminum alloys. However, a detailed analysis of the morphology and propagation of pitting corrosion was not carried out; in fact, the authors concentrated their discussion on the electrochemical results.

On the other hand, Ren and Zuo[16] and Takahashi et al.[13,14] focused their analyses on explaining the corrosion mechanism when pure anodized Al (99.99%) was subjected to an anodic polarization test in NaCl solution. The authors mainly focused their attention on the mechanism of corrosion without resorting to different techniques for the characterization of the morphology and the extent of pitting corrosion. Moutarlier et al.[17] investigated the corrosion resistance of a commercial alloy (AA2024) anodized in different anodizing baths and discussed their results qualitatively. Although this work[17] demonstrated the extent of the corrosive attack by cross-sectional images, the images presented did not allow evaluation of the actual extent of the attack, suggesting that the methodology may not be suitable.

It is important to point out that to analyze the depth and extension of the corrosive attack on Al alloys, different methodologies have been used and reported in the literature, such as optical microscopy (OM) and optical profilometry (OP) from the surface and analysis by OP and scanning electron microscopy (SEM) in metallographic cross-sections. However, some works have shown that the results obtained by OP can lead to misinterpretations,[18–29] once that, by this technique the calculation of the surface profile is carried out from the distortion of a regular shape light pattern projected on the surface.[26] Therefore, different results can be obtained depending on the condition of the surface such as accumulation of corrosion product or even depth limitation.

The preparation of samples for the analysis of corrosion attack in cross-section is complex, and only a few laboratories have access to the ultramicrotomy technique, which is a precise technique.[30] The more accessible experimental techniques include embedding the samples in phenolic or acrylic resin followed by cutting with a diamond disk and then polishing the sample in the cross-section, although the methodology adopted for sample preparation in many studies is not precisely described. Therefore, the results obtained for the corrosion attack might be inaccurate, depending on the methodology used for evaluation, as in the case of Moutarlier et al.[17] In their work, it was not possible to identify the real depth of the attack associated with pits. Thus, establishing a methodology to validate the results of OP and cross-sectional analysis is of great importance.

Although there is an ASTM standard[31] that addresses most of these concerns, the standard is quite general and takes into account the assessment of pitting corrosion for corroded metal samples without specifying the type of material and without distinguishing the possible misinterpretations that may arise when different techniques are used. In addition, depending on the material to be studied, its microstructural characteristics can lead to different corrosion mechanisms and, consequently, different morphologies in the propagation of pitting corrosion. For example, for anodized Al alloys, few works[13–17] proposed the corrosion mechanism based on microstructural characterization using different techniques. Therefore, in the present study, a simple methodology is proposed for pitting evaluation in anodized Al alloys. The aim is to obtain accurate data for evaluating the extent of corrosion attack at the surface and in-depth.

2 | EXPERIMENTAL

2.1 | Adopted experimental methodology

The methodology used in this study is schematically illustrated in Figure 1, which shows the following:

(1) The characteristics of the samples used in this study.
(2) The metallographic preparation procedure (grinding and polishing) adopted before anodizing.
(3) The anodizing procedure in tartaric sulfuric acid (TSA) solution.[32,33]
(4) The setup adopted in the electrochemical tests corresponds to open-circuit potential (OCP) measurements, followed by potentiodynamic polarization in 0.1 mol L^{-1} NaCl solution.
(5) The sites associated with pitting corrosion after polarization following the steps: (a) choice of the pits on the surface for observation using OM and OP and SEM in the backscattered electron (BSE) and secondary electron (SE) detector modes, after that (b) cutting the samples at the cross-section, close to the pit, followed by grinding and polishing and observation using SEM. SEM in BSE mode was used to compare the same methodology used in pitting corrosion studies on Al alloys.[13–17]

2.2 | Material

AA7475 aluminum alloy in the form of a rolled sheet with a thickness of 1.6 mm was used. The chemical composition of the alloy is given in Table 1.

2.3 | Anodizing procedure

Samples with a diameter of 15 mm were metallographically prepared by grinding with silicon carbide (SiC) paper up to #P4000 and polished with 1 μm diamond suspension. The metallographic preparation was carried out

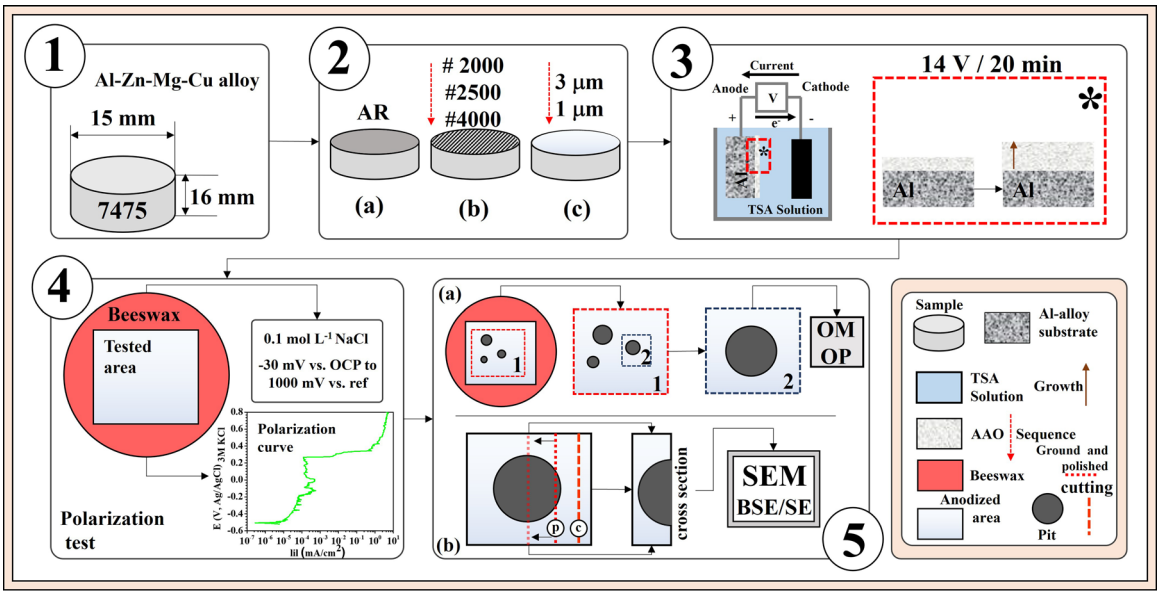

FIGURE 1 Schematic illustration of the experimental procedure adopted in this study: (1) description of the as-received (AR) sample; (2) sample preparation before anodizing process; (3) experimental setup of the anodizing process in sulfuric tartaric anodizing solution (TSA); (4) experimental setup used in anodic polarization tests; and (5) methodology used for characterization of the corroded sites generated by anodic polarization, of the top surface and cross-section view. BSE, backscattered electron; OAA, anodic aluminum oxide; OCP, open-circuit potential; OM, optical microscopy; OP, optical profilometry; SE, secondary electron. In step 2, the sample surface (a) as-received; (b) after the grinding process; and (c) after the polishing process, are illustrated. Whereas, in step 5 the methodology to evaluate pitting corrosion on the (a) surface) and (b) cross-section. [Color figure can be viewed at wileyonlinelibrary.com]

TABLE 1 Chemical composition of the alloys (wt%) obtained by inductively coupled plasma optical emission spectrometry.

Elements	wt%
Al	Balance
Cu	1.52 (1.2–1.9)
Mg	1.90 (1.9–2.6)
Mn	0.02 (≤0.06)
Fe	0.07 (≤0.12)
Zn	6.10 (5.2–6.2)
Si	0.03 (≤0.12)

Note: Values in parentheses present the composition specification according to ASM[34] for the AA7475 aluminum alloy.

before anodizing to guarantee a homogeneous surface without the presence of the near-surface deformed layer (NSDL), which is introduced to the alloy surface during the manufacturing process.[35] According to the literature,[36–39] the NSDL has different chemical/metallurgical characteristics compared to the bulk alloy, such as Mg-rich bands, ultrafine and dynamically recrystallized grains, second phase, finely and well-distributed particles at the grain boundaries, oxides at the grain boundaries, and cracks. The NSDL especially affects the in-service performance of the wrought alloy after the anodizing process.[35] Therefore, some authors use pretreatment steps before the anodizing process, such as acid/alkaline degreasing, or mechanical polishing (metallographic preparation).[1,5,40] In this work, metallographic surface preparation was used to compare our results with those of works already reported in the literature.[41,42]

Anodizing was performed in TSA solution composed of 0.46 mol L^{-1} sulfuric acid and 0.53 mol L^{-1} tartaric acid at 37 ± 1°C using a potentiostat (SP-300 from BioLogic). The area exposed to the TSA electrolyte was 1 cm^2. The Al alloy samples were used as working electrodes, and a platinum mesh, with an area of 4 cm × 10 cm, was used as the counter electrode. The volume of the TSA solution was 550 mL, and the distance between the working electrode and the counter electrode was 7 cm. Anodizing was performed for 20 min under constant voltage at a potential difference between the working and the counter electrode of 14 V to obtain oxide layer thickness between 1.5 and 10 µm.[43]

The cross-section of the films formed through the anodizing procedure was analyzed using a Hitachi Tabletop Microscope TM3000 operating at an accelerating voltage of 20 kV. For this, the anodized samples were embedded in phenolic resin as a sandwich and then cut in their central line and metallographically prepared as described earlier.

2.4 | Electrochemical corrosion test

The corrosion resistance of the anodized AA7475 aluminum alloy samples was evaluated by electrochemical measurements using a BioLogic SP-200 potentiostat. Electrochemical measurements were performed in 0.1 mol L^{-1} NaCl solution using a three-electrode setup with the anodized alloy samples as working electrodes, an Ag/AgCl (3 M KCl) as reference electrode, and a platinum wire as counter electrode. It is important to highlight that seven polarization curves were performed using a new sample for each measurement. The exposed surface of the working electrode was delimited to 0.25 cm^2 by using beeswax to avoid crevice corrosion. Anodic potentiodynamic polarization tests were performed in the direction of nobler potentials with a scan rate of 1 mV s^{-1} starting at −30 mV, relative to OCP, and finishing at a potential of 1000 mV versus Ag/AgCl (3 M KCl).

2.5 | Pits examination

After electrochemical tests, the formed pits were analyzed by OM in bright field and OP using a Leica DMLM-EC3 and a ZeGage equipment from Zygo, respectively. The pits were also examined through OM and OP after the removal of the corrosion products and anodic layer by immersion of the tested samples in a solution containing 20 g of CrO_3 + 30 mL of H_3PO_4 in 1 L of deionized water at 60°C for 3 min, known as desmutting solution.[44] Next, the samples were immersed in distilled water using an ultrasonic bath for 20 min and then dried in a stream of cool air. The samples were prepared for observation of the cross-section by cutting in the cross-section near the pits, followed by grinding and polishing. Cutting was carried out using a Minitom™ precision cutting machine with a M1D13 127 mm diamond cut-off from Struers. The samples were ground with SiC paper to #P4000 and polished with 3 and 1 μm diamond suspensions until reaching the center of the pits. Finally, the prepared surfaces were observed by SEM using a Hitachi Tabletop Microscope TM3000 operating at an accelerating voltage of 20 kV. Energy-dispersive X-ray spectroscopy (EDS) maps were performed operating at an accelerating voltage of 20 kV.

Subsequently, the data of depth and extension of pitting attack on the surface and cross-section were compared. The statistical data on average pit diameter and depth were constructed from the comparison of the corrosion attack measured on the surface and in the cross-section. Two largest pits per sample were analyzed for both samples.

3 | RESULTS AND DISCUSSION

3.1 | Characteristics of the anodic aluminum oxide (AAO) formed by anodization in TSA solution

Figure 2 shows the main characteristics of the Al alloy after anodizing in TSA solution. Figure 2a,b shows a cross-sectional image of the anodic layer and the top surface, respectively. The continuity of the anodic layer can be observed in Figure 2a, and also the presence of the porous layer (Figure 2b). At higher magnification (Figure 2c), it can be seen that the thickness of the anodic layer was 4.8 ± 0.1 μm. Similar anodic layer thicknesses obtained by TSA anodization have been reported in the literature.[41,45] Moreover, the resulting film thickness is in accordance with patent specifications.[43]

Figure 2d,e shows the same surface area of the alloy before and after the anodizing process. It is important to mention that the microstructure of Al alloys is composed of intermetallic particles (IMPs), as indicated by the blue arrows (Figure 2d). In the AA7XXX series, it is well reported that IMPs tend to have a greater amount of Cu and Fe in their composition compared to the matrix,[46–50] and this was also observed with the samples of this study, as shown in Figure 2d. Fe is present in Al alloys as an impurity from the bauxite mining process, raw material for alloy production, and due to the casting process.[51] Cu is added as an alloying element to improve the mechanical properties of the material.[52] The addition of Cu (>1 wt%) favors the formation of these phases.[53] It is very difficult to remove all IMPs formed during the manufacturing process from the alloy surface and it is economically unfeasible.[51,54] These particles are indicated by the arrows in Figure 2d and tend to appear isolated or clustered on the alloy surface.

It is noteworthy that IMPs have a different electrochemical potential compared to Al matrix due to their chemical composition; thus, the connection between matrix and IMPs might lead to galvanic microcells that promote corrosion initiation.[55] In fact, during the anodizing process, IMPs tend to dissolve and form voids on the surface of the anodic layer, as indicated by the red arrows in Figure 2e–g.[42,56] Saenz De Miera et al.[57] reported similar results when studying the behavior of IMPs in the AA7075-T6 aluminum alloy during sulfuric anodizing. In addition, changes in the morphology of the film have been reported.[41,42] In recent work from our group,[58] it was observed that the average depth of the cavities formed was 2.6 ± 1.3 μm for the same alloy anodized under similar anodizing conditions.

Interestingly, after anodizing, grain boundaries were seen on the film surface by OM, as shown in Figure 2h,i.

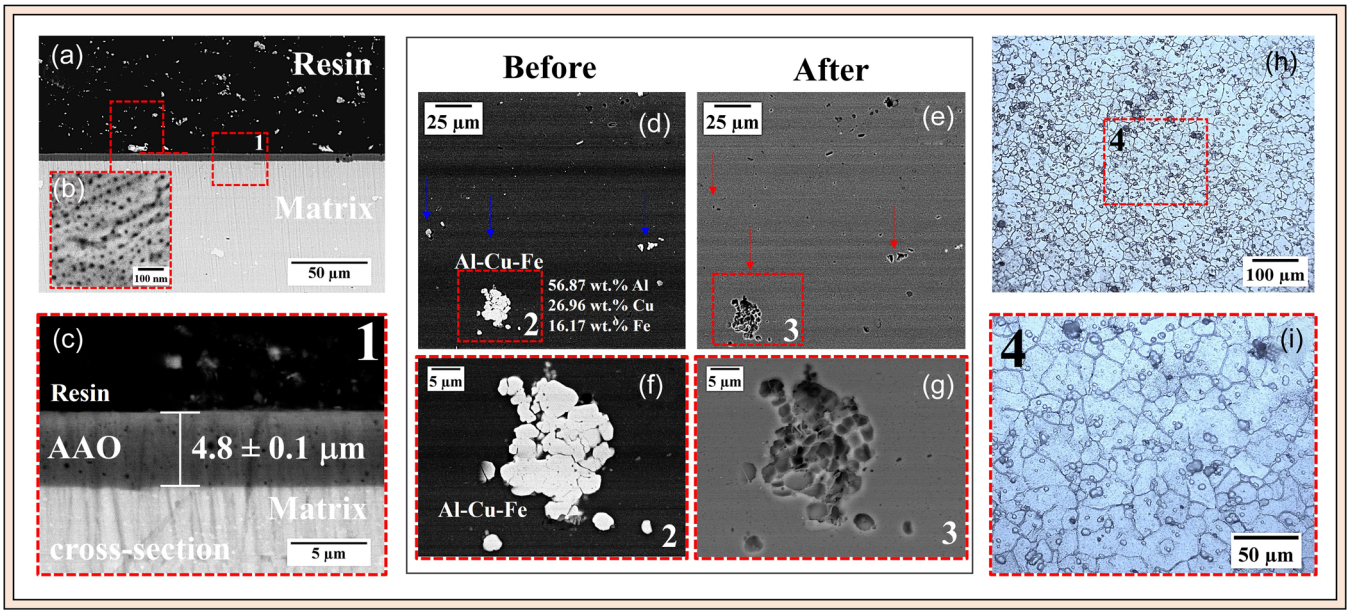

FIGURE 2 Micrographs of the AA7475 anodized aluminum alloy in tartaric anodizing solution (TSA) solution: (a) cross-section scanning electron micrograph of the Al alloy after anodization; (b) scanning electron micrograph of the Al alloy surface after anodization; (c) higher magnification of the dashed squared region shown in (a); (d, e) scanning electron micrographs of the Al alloy surface before and after TSA anodization, respectively; (f, g) higher magnification of the dashed squared regions shown in (d, e); (h) optical micrograph of the Al alloy surface after anodization test; and (i) higher magnification of the dashed squared region shown in (h). The blue and red arrows shown in (d, e) indicate the micrometric intermetallic particles and the voids caused by their dissolution during the anodizing process, respectively. All scanning electron micrographs were obtained in backscattered electron mode. AAO, anodic aluminum oxide. [Color figure can be viewed at wileyonlinelibrary.com]

Anodizing is often used to reveal grain structure of Al alloys since the anodic oxidation behavior of grain boundaries is different from the alloy matrix.[59] According to Runge,[60] the oxidation behavior of the grain boundaries in AA7xxx alloys is influenced by preferential oxidation of η ($MgZn_2$) at the grain boundaries. As the film is translucid, it was possible to observe the under-film grain boundaries by OM. It is worth mentioning that this type of behavior strongly depends on the alloy and the thickness of the anodic film. For example, foundry Al alloys have a large number of Si precipitates in their microstructure.[61] These precipitates do not dissolve during anodizing. Thus, they might be incorporated into the oxide layer, resulting in the formation of a gray anodic layer. On the other hand, the color of the anodic layer on the AA6063 aluminum alloy depends on the applied voltage due to the preferential oxidation of the β′ phase (Mg_2Si).[62,63] This explains why each Al alloy needs a specific investigation once the anodizing behavior of these alloys varies according to their composition.

The difference in observations by SEM (Figure 2e–g) and OM (Figure 2h,i) can be explained by the formation of images by both techniques. For example, as the anodic layer on the alloy under study is translucid, the grains of the alloy (revealed due to oxidation of the η ($MgZn_2$) phase) below the oxide film can be observed by OM. This happens because the incident white light in OM passes through the film,[64] whereas by SEM there is interaction between the primary electron beam and the sample.[65] It is known that by SEM it is possible to obtain images by secondary and BSEs. SEs have low energy and interact with the last atomic layers of the materials, forming topography images. On the other hand, BSEs have high energy with intensity dependent on the atomic weight.[65,66] Thus, bright regions correspond to heavy atomic elements, and dark regions correspond to light ones.

3.2 | Pitting introduced by potentiodynamic polarization

Figure 3 displays the potentiodynamic polarization curves for the anodized aluminum alloy studied in this investigation.

The results showed that there was variability in the breakdown potential of the anodic layer. In some cases, the breakdown occurred at potentials lower than +0.1 V (curves 3, 4, and 7) and in others at higher potentials (curves 1, 2, 5, and 6). Pseudo-passivity was observed in the polarization results indicated by the current density plateau that, for some samples, was at approximately 10^{-5} mA/cm^2 (curves 1, 2, 5, and 6) while, for others, it was nearly 10 times higher

(curves 3 and 7). These results show the variability in the characteristics of the anodic layer formed. The increase in current density at different polarization potentials is due to the "pseudo-passive film" breakdown. This behavior is similar to the breakdown of the naturally formed oxide film. The thicker oxide layer produced by anodizing increases the time for corrosion to start by delaying the access of aggressive species to the substrate exposed underneath the defective regions of the anodic layer.

For the anodized condition in aerated media and in the presence of chloride ions (Cl^-), it was possible to observe the "pseudo-passive" region, whereas for Al alloys in the bare condition, the passive region can only be observed in deaerated media or in aerated media containing Cl^- ions.[18] The increase in time until passive film breakdown depends on the thickness of the anodic layer, the electrolyte used for anodizing, and the defects in the film, as shown in Figure 2e–g. It is important to highlight that the anodic layer might be highly defective, as was the case of one of the tested samples (curve 4). For this sample, surface observation after polarization showed a high density of defects, greater than the other samples tested (Figure 4).

At potentials of approximately +0.3 V, the current density reached values around 1 mA/cm^2 (curves 1–5 and 7), while for curve 6, this range of current density was only observed at potential superior to +0.6 V. This behavior is widely observed in the polarization of Al alloys in Cl^- media, being characterized by diffusion control of Al^{3+} species, besides ohmic drop effect within the pits.[67–71]

After the test, the surface of the alloy was examined (Figure 4). Pits were observed on the tested surface, as indicated by the red arrows. Two pits per sample were characterized, as described in the next section.

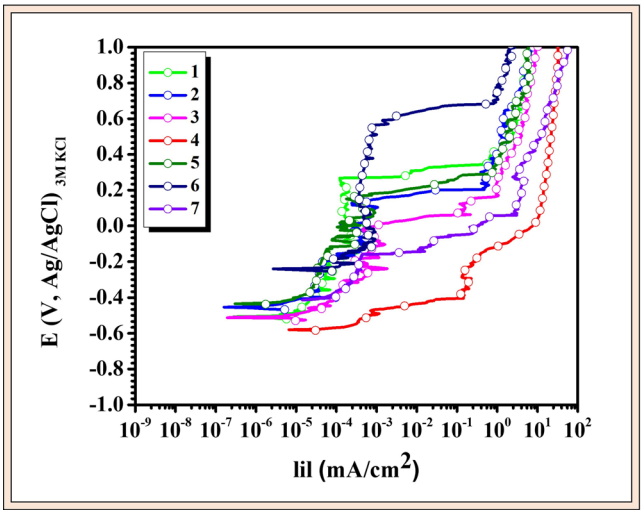

FIGURE 3 Anodic potentiodynamic polarization curves of the AA7475 anodized aluminum alloy obtained after 5 min of immersion in 0.1 mol L^{-1} NaCl solution. [Color figure can be viewed at wileyonlinelibrary.com]

3.3 | Evaluation of the corrosion attack in the anodized Al alloy by using OM, OP, and SEM after potentiodynamic polarization

Figure 4 shows the surface of the anodized AA7475 alloy samples after polarization tests and the corresponding pits formed. Figure 4a shows the surfaces corresponding to the polarization curves presented in Figure 3. Pits are observed

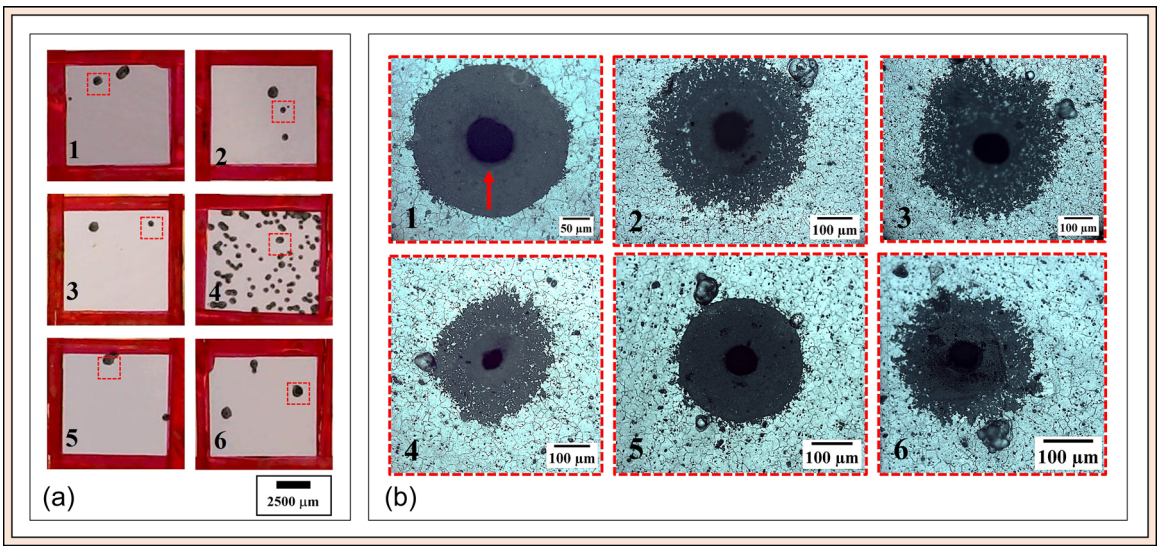

FIGURE 4 (a) Surface macrographs of the AA7475 anodized aluminum alloy after polarization test in 0.1 mol L^{-1} NaCl solution and (b) micrographs corresponding to the dashed squared area shown in (a). The surfaces shown in (a) correspond to the polarization curves shown in Figure 3. The red arrows indicate the pit formed after the polarization. [Color figure can be viewed at wileyonlinelibrary.com]

on all samples. At higher magnifications (Figure 4b), the morphology of the pits is a black spot surrounded by a "dark region," as indicated by the red arrow.

The depth of attack associated with these pits (Figure 4b) was evaluated by OP. Some pits are shown in Figure 5. Values of the order of 100 μm were observed. This confirms that corrosion propagates in the substrate below the anodic layer (as shown in Figure 2c). The thickness of the film was 4.8 ± 0.1 μm. Corrosion starts at the defects in the anodic layer (oxide). Therefore, the pits shown in Figure 4 are the initial "weak points" of the anodic layer, such as the defects shown in Figure 2e–g. According to Ren and Zuo,[16] these pits tend to provide a diffusion channel through which ion exchange, between inside and outside of the pit, can take place. In fact, during the polarization test, it was possible to observe hydrogen evolution at these defective areas, at potentials close to that corresponding to the increase in current observed in the polarization curves (Figure 3).

Attack below the anodic layer was confirmed through elemental chemical analysis carried out in the pitted area (Figure 6) after the polarization test. Figure 6a shows the surface of the sample corresponding to curve 4 after the polarization test, as shown in Figure 3. Figure 4b presents a pit indicated by the red dashed square in Figure 4a and its respective EDS maps. It is observed that the developed pits had high contents of Al, Cu, Fe, and Zn and low concentrations of oxygen in their interior. The presence of Cu indicates enrichment of this element inside the pits, which was due to great electrochemical activity in these regions. Copper enrichment/redeposition close to the anodic sites has been reported.[41,42,58] Similar results were also reported by Moutarlier et al.[17] when studying the corrosion behavior of alloy AA2024-T3 anodized in sulfuric acid (H_2SO_4).

It is important to emphasize that the analysis obtained by the EDS maps is a semiquantitative analysis[72]; therefore, it only indicates which element is in greater quantity in relation to the other, explaining the greater amount of oxygen in the region associated with the anodic layer composed mainly of Al_2O_3.

It is important to highlight that the anomalous contrast around the pit, indicated by the red arrow (Figure 6b), occurs due to surface charging, as it occurs during the acquisition of the EDS maps with the electron beam operating at 20 kV and focused in these regions for 30 min, causing these artifacts.[73] It is worth noting that charging is very common for anodized alloys, as the anodic layer has low conductivity, leading to the accumulation of electrostatic charges on the sample surface. One way to avoid this type of artifact when analyzing images of anodized alloys is to use low acceleration voltage during image acquisition. For anodized Al alloys, for example, 1–3 kV is recommended[41,74,75]; however, at this voltage, it would not be possible to excite specific elements and satisfactorily measure the resulting X-rays.[72,76,77]

The pits diameter (black holes) in Figure 4 were all inferior to 70 μm. However, some pits showed different

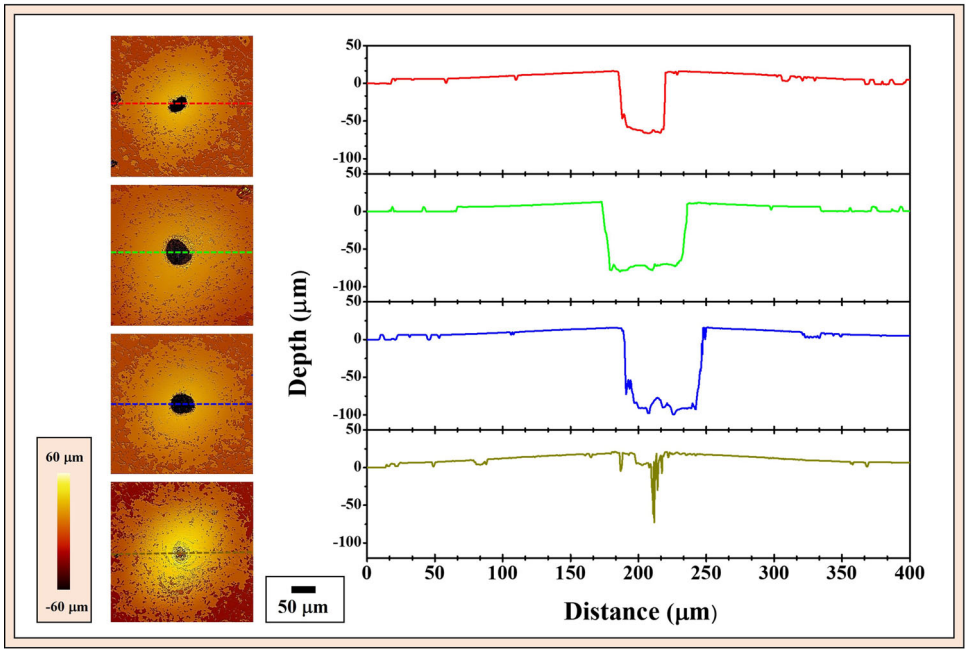

FIGURE 5 Optical profilometry measurements performed on pits formed in AA7475 anodized aluminum alloy after anodic polarization in 0.1 mol L^{-1} NaCl solution. [Color figure can be viewed at wileyonlinelibrary.com]

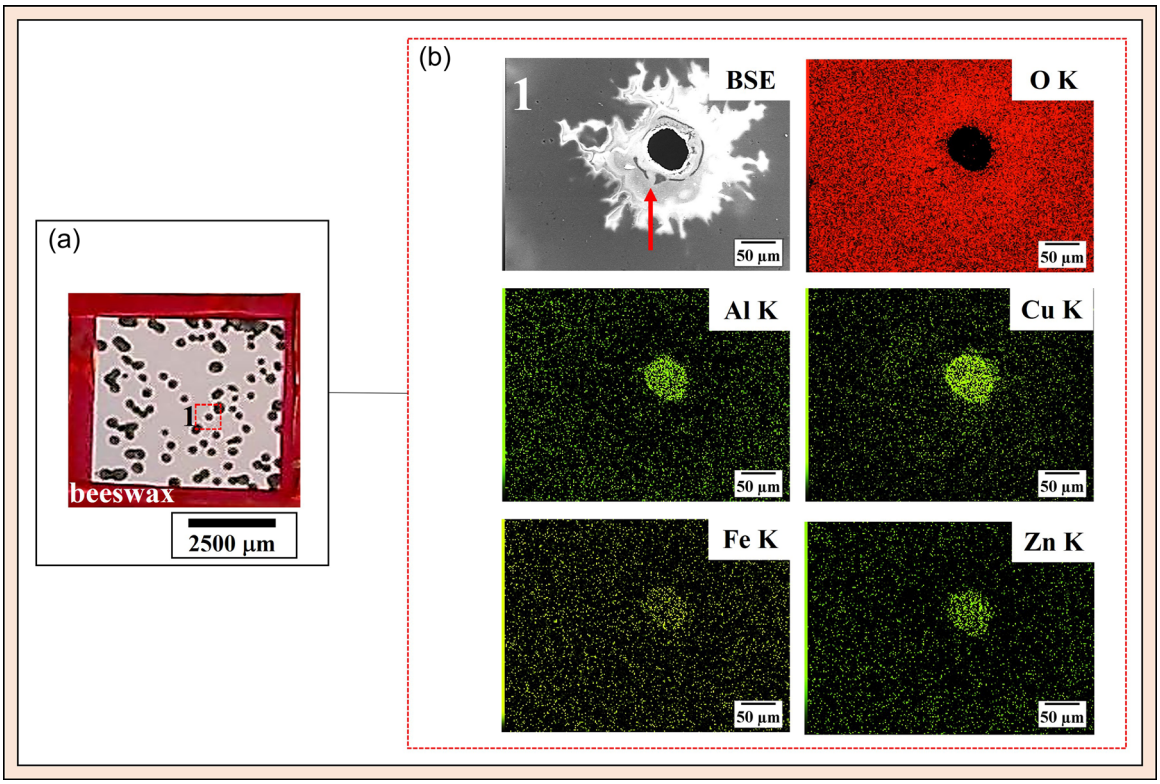

FIGURE 6 Micrographs corresponding to a pit in the AA7475 anodized aluminum alloy after anodic polarization test in 0.1 mol L^{-1} NaCl solution: (a) surface macrography (corresponding to polarization curve 4 shown in Figure 3) and (b) energy-dispersive X-ray spectroscopy micrograph maps of the dashed squared region shown in (a). Scanning electron micrographs were obtained in backscattered electron (BSE) mode. A red arrow in (b) indicates charging around the pit, thus giving rise to anomalous contrast. [Color figure can be viewed at wileyonlinelibrary.com]

attack extension. This suggests that the real size of the pits in Figures 5 and 6 may differ, which might lead to misinterpretations, as shown in Figure 7.

In Figure 7a, a small pit (red arrow) and a large pit (blue arrow) measuring nearly 100 µm are observed. Due to the limitation of the OM, it is not possible to observe the characteristics within these pits, but it is possible to see regions with different focus and a black region surrounding the pits. To get a detailed characterization of these regions, SEM was also used, as shown in Figure 7b,c. In both BSE and SE modes, the "dark region" surrounding the pits shown in the OM image was not observed. Additionally, swelled regions related to the anodic layer were observed. This leads to out-of-focus regions in the OM images. The same contrast observed in the black region surrounding pits, observed by OM, and the remaining anodic layer suggests that this black region corresponds to a corroded pattern below the anodic layer. Since the anodic layer is translucent, the white light beam passes through the film revealing the corrosion pattern below the film, as shown by OM image, as it was also observed for the grain boundaries, as described earlier. On the other hand, for the SEM images, as the electron beam interacts with the anodic layer, contrast was the same over all the anodic layers that remained after corrosion, and in this case, the corrosion pattern below the film could not be observed. Other corrosion features, such as morphology, were also observed by SEM. Figure 7d shows a large cavity measuring approximately 150 µm. In the cases where small pits were not observed, the anodic layer presented a large detached area. This results from voluminous corrosion products between the substrate in the anodic layer lifting it up. The crystallographic morphology of the matrix attack was observed by SEM (Figure 7e,f).

Figure 8a shows a pitted region surrounded by bubble-like structures (deposited corrosion products below the anodic layer), as indicated by the red arrows. At higher magnifications (Figure 8b), the pit can be seen, and a very dark contrast inside it suggests that this region must have a great depth. Image at higher magnifications of this region in SEM-SE mode (Figure 8c) displays the accumulation of corrosion products within the pits, as indicated by the blue arrow. Furthermore, it is observed that the regions surrounding the pit have some cracks, indicated by the yellow arrows. This result suggests that the accumulation of corrosion products below the film leads to increased

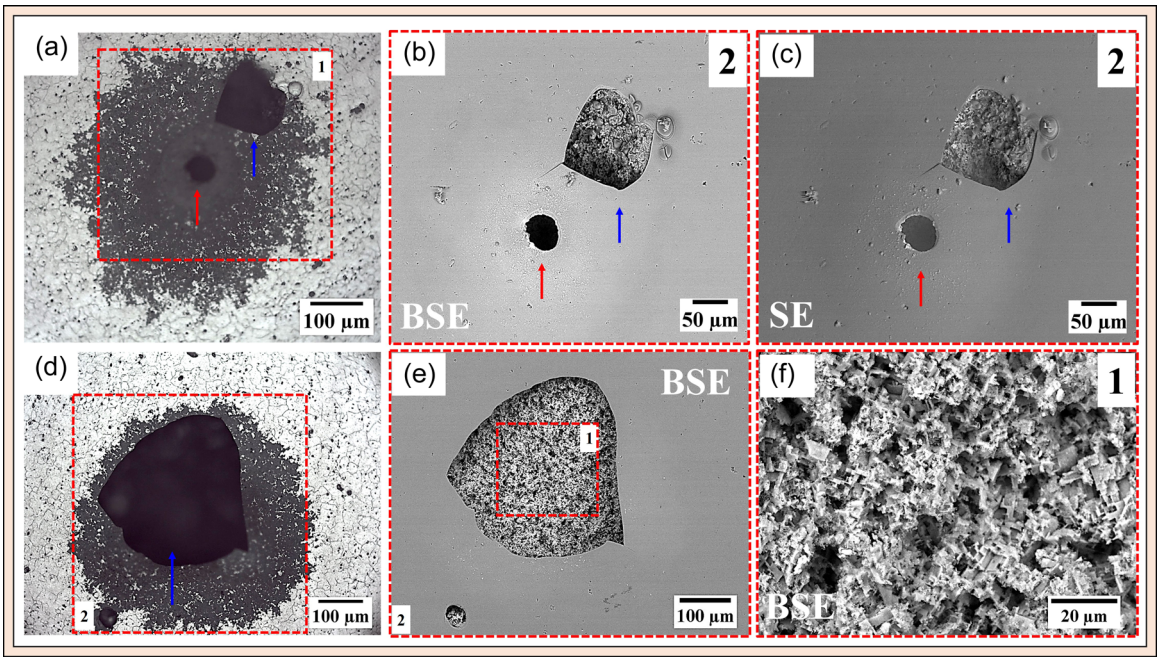

FIGURE 7 Micrographs corresponding to pits in the AA7475 anodized aluminum alloy after anodic polarization test in 0.1 mol L^{-1} NaCl solution: (a) optical micrograph; (b, c) scanning electron micrographs corresponding to the pit shown in (a) obtained by backscattered electron (BSE) secondary electron (SE) mode; (d) optical micrography of another pit; (e) scanning electron micrograph corresponding to the pit shown in (d); (f) higher magnification scanning electron micrograph of the dashed squared region shown in (e); the red and blue arrows indicate the pit opening after the polarization test and fallen anodic layer, respectively. [Color figure can be viewed at wileyonlinelibrary.com]

stress on it. Furthermore, these cracks can propagate to regions adjacent to the pits, as shown in Figure 8d. It is possible to observe structures similar to bubbles in the anodic film. These results show that the corrosion products are not only present in the regions corresponding to visible pits at the outer surface (Figure 8c), suggesting that the real extent of pitting is masked. It is noteworthy that the swelling of the anodic layer cannot be observed by OM due to a lack of focus in these regions. In the cross-section of the black regions surrounding the pits, corrosion product accumulation under the anodic layer is evident (Figure 9).

Figure 9a presents a view of a cross-section region in which corrosion products accumulated over and below the anodic layer, as observed in Figure 8. At higher magnifications (Figure 9b,c), corrosion products can be observed below the anodic layer, as indicated by the red arrows. This leads to osmotic pressure inside the pits and then to "swelling" in the anodic layer (indicated by the blue arrow). Furthermore, it can cause propagation of cracks in the film, as seen in Figure 8, and then to its rupture. These phenomena explain the discontinuity of the black region surrounding the pits with dimensions inferior to 70 µm (Figure 7a), or the total absence of small holes revealing corroded areas with extension superior to 100 µm (Figure 7d). It is noteworthy that this type of under-film corrosion behavior is commonly observed in the development of filiform corrosion in Al alloys[78,79] and corrosion in thin films.[80–82]

A comparison between the corrosion morphology of the surface, before and after the removal of the corrosion products and the anodic layer, must be carried out to observe the real extent of the attack, as shown in Figure 10.

Figure 10a shows an OM image of a pit (indicated by the red arrow) after potentiodynamic polarization, and Figure 10b,c presents scanning electron micrographs of the pit in Figure 10a. At higher magnifications (Figure 10d), the morphology of the pit and its size can be observed. After the removal of the anodic layer and corrosion products beneath the film, different morphologies are observed. By OM (Figure 10e), it can be seen that the real extension of the pit is associated with the black region surrounding the pits, with sizes lower than 70 µm; however, due to its limitations, it is not possible to evaluate the morphology and depth of the attack within the pit due to difficulty in focusing, as indicated by the arrow. BSE and SE analysis, Figure 10f,g, are useful in these observations once attack on the alloy matrix is observed. The characteristics such as contrast difference observed in Figure 10g within the pit show that it penetrated deep into the alloy.

Interestingly, the results in Figure 10 show that depending on the adopted methodology different information can be obtained. In fact, the pit observed in

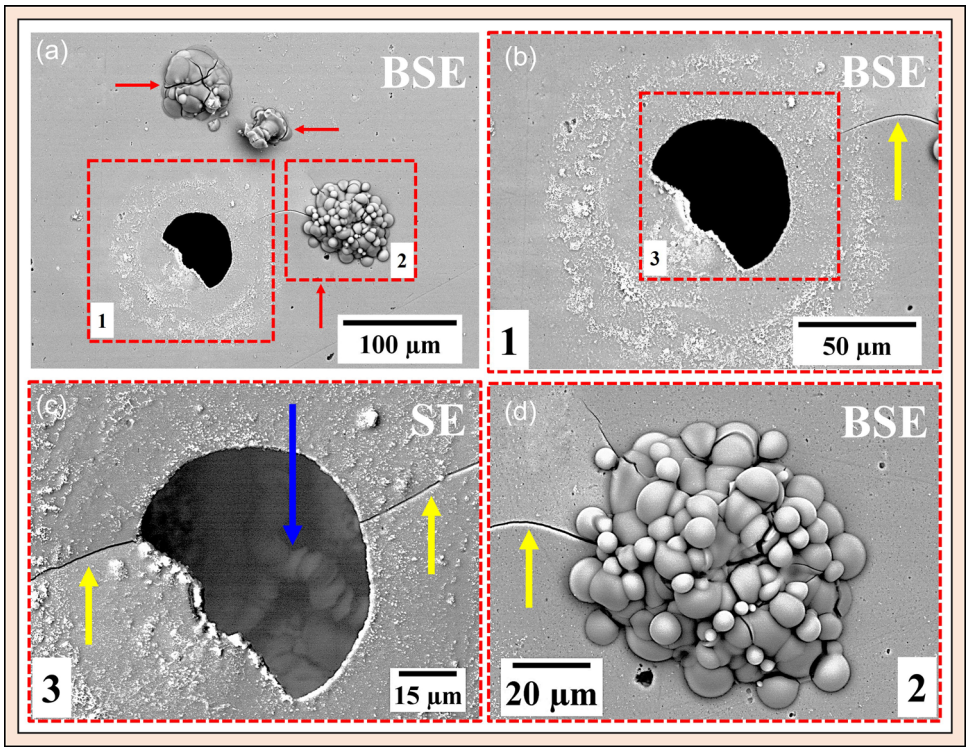

FIGURE 8 Scanning electron micrographs of the surface of the AA7475 anodized aluminum alloy after anodic polarization test in 0.1 mol L^{-1} NaCl solution: (a) micrograph corresponding to the pit on the surface; (b) higher magnification of the dashed squared region shown in (a); (c) higher magnification of the dashed squared region shown in (b); and (d) higher magnification of the dashed squared region shown in (a). The red and blue arrows indicate the swelling of the anodic layer and the accumulation of corrosion products beneath the film, respectively. The yellow arrows indicate the cracks present in the anodic layer. Figures (a), (b), and (d) were obtained in backscattered electron (BSE) mode, whereas (d) was obtained in secondary electrons (SE). [Color figure can be viewed at wileyonlinelibrary.com]

Figure 10a–c does not show the extension as seen in Figure 10e–g. Therefore, the results reported by Zuo et al.,[15] Ren and Zuo,[16] and Moutarlier et al.[17] presented misinterpretations about the true extension of pitting seen on the surface of anodized Al alloys.

The results presented in Figures 4–10 show that evaluation of pitting from the surface of anodized Al alloys must be carried out with care, being necessary to carry out cross-sectional characterization as a complementary technique.

3.4 | Pits observation in anodized Al alloy: Analysis through surface and cross-section

After the polarization test, some pits were analyzed, as shown in Figure 11. Figure 11a shows the surface of the sample after the polarization test. The images obtained by profilometry and OM from the pit, highlighted by the red dashed square (Figure 11a), are shown in Figure 11b–d. In the first analysis, small openings were observed due to pitting on the substrate, with dimensions of 67.6 ± 16.2 µm, as seen in Figures 4, 5, and 8. However, after removing the anodic layer, it was observed that the pit sizes observed did not reflect the actual extent of the attack in the alloy. Indeed, the pits had an opening with an average diameter of around 290.8 ± 84.1 µm. Therefore, a difference of about 200 µm in diameter in the extent of the attack was noted between the measurements from film surface and from the corroding alloy beneath the film, which is illustrated in Figure 11d.

These results show that the measured extent of corrosion using various techniques greatly differs when the observation is made from the top of the sample without the removal of corrosion products and anodic layer. These characteristics become more evident when analyzing the depth profile obtained by OP before and after removing the corrosion products and anodic layer, as shown in Figure 11e. It is seen that the depth of the attack estimated before the removal of the anodic layer and corrosion products (green line) does not correspond to the real extent of the attack. However, after the removal of the anodic layer and corrosion products, the depth and width of the attacked area (pits) can be easily observed (blue line). The SEM image in Figure 11e

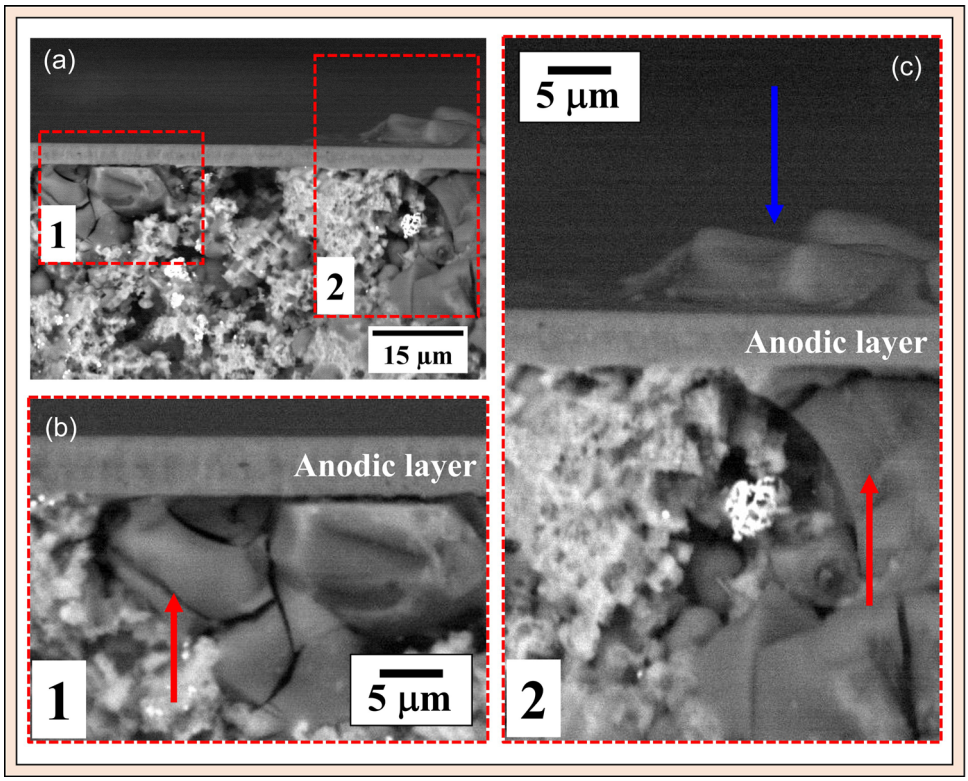

FIGURE 9 Scanning electron micrographs of the cross-section of the AA7475 anodized aluminum alloy after anodic polarization test in 0.1 mol L^{-1} NaCl solution: (a) cross-section; (b, c) higher magnification of the dashed squared region shown in (a). The red and blue arrows in (b) and (c) indicate the corrosion product beneath the anodic layer and the swelling of the film, respectively. [Color figure can be viewed at wileyonlinelibrary.com]

confirms these observations and validates the result obtained by profilometry described in Figure 11d. The results show that the pits propagate and grow below the oxide layer and that the small pits (black spots shown in Figure 4) in the anodic layer provide a diffusion channel through which ion exchange takes place between the interior of the pit and the outside.

Figure 12 presents statistical data on the average diameter and depth of pits before and after the removal of corrosion products by desmutting. Before desmutting, the pit's mouth showed nearly 25% of its actual size measured after desmutting (Figure 12a). Also, before the removal of corrosion products, the estimated depth of corrosion penetration was nearly 60% of the depth measured after desmutting (Figure 12b). The mean depth estimated considering 14 pits before and after desmutting was 79.4 ± 13.4 and 144.4 ± 12.8 µm, respectively.

The observations of this study show that it is very important to be aware when evaluating pit dimensions from the surface that the presence of corrosion products deposited in the pits and surrounding them must be considered, and these affect the extent and depth of the attacked area as revealed by cross-section analysis. The use of techniques such as OP measurements can lead to misinterpretations. It is noteworthy that, although the results were validated by cross-sectional imaging, many Al alloys corrode along grain boundaries and the depth of the attack cannot be estimated by OP. Despite this, OP presents some advantages for the evaluation of corrosion in Al alloys. For example, Schmidl et al.[26] studied the formation of pits in the bare AA2024-T3 Al alloy and showed that the undercuts on the left flank of the pits could not be measured by means of 3D pattern profilometry or laser scanning microscopy. Cross-sectional analysis would be required to not omit certain regions in the pits. In our study, this was not observed because the developed pits presented an elliptical shape. However, depending on the alloy studied, the prospect of intergranular attack must be taken into account. This shows that each specific type of Al alloy needs its specific investigation since, depending on the type of alloy, different mechanisms of corrosion might be operative.

Other techniques such as atomic force microscopy (AFM) could also be used, but there are concerns about the effectiveness of this method due to the limitation of contact between the AFM microprobe and the pit bottom[83,84] To overcome the limitations related to AFM, in recent decades the near-field scanning OM (NSOM) technique has been developed, which allows to work with standard optical tools integrated with AFM.[85]

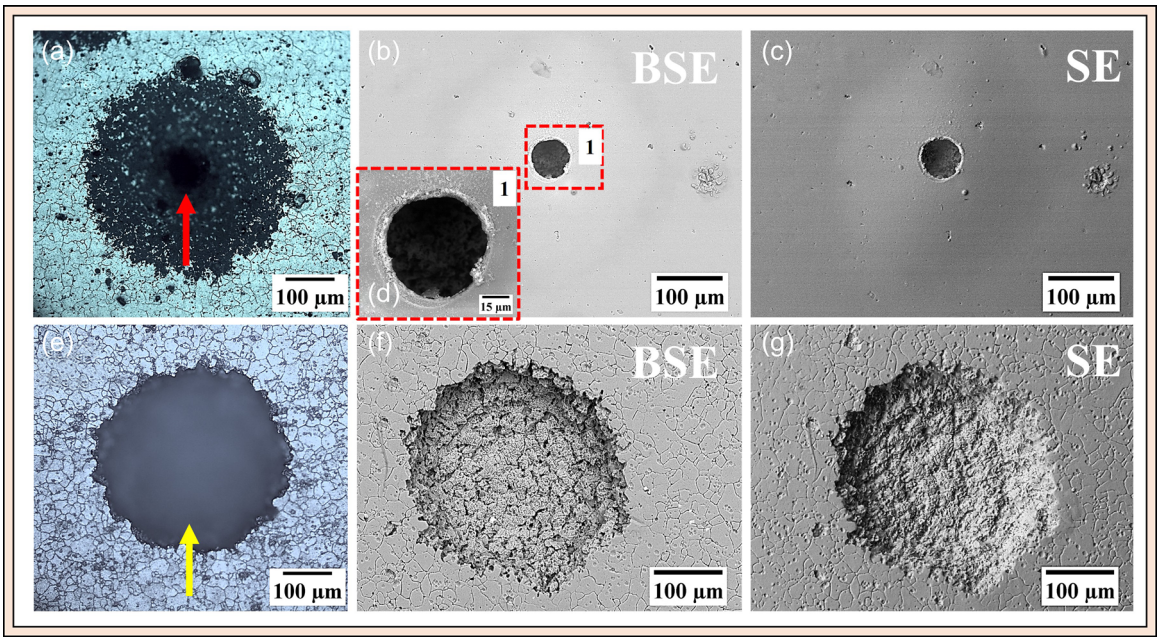

FIGURE 10 Micrographs corresponding to a pit in the AA7475 anodized aluminum alloy after anodic polarization test in 0.1 mol L^{-1} NaCl solution: (a) optical micrograph of pitting corrosion before the removal of corrosion products and the anodic layer; (b, c) scanning electron micrographs corresponding to (a); (d) higher magnification of the dashed squared region shown in (c); (e) optical micrograph of pitting corrosion after the removal of corrosion products and the anodic layer; and (f, g) scanning electron micrographs corresponding to (e). The red arrow in (a) indicates pitting before the removal of the anodic layer and corrosion products, while the yellow arrow in (e) indicates the lack of focus to analyze the real extent and depth of pitting after the removal of the corrosion products and anodic layer. Figures (b), (d), and (f) were obtained in backscattered electron (BSE) mode, (c) and (g) were obtained in secondary electron (SE) mode. [Color figure can be viewed at wileyonlinelibrary.com]

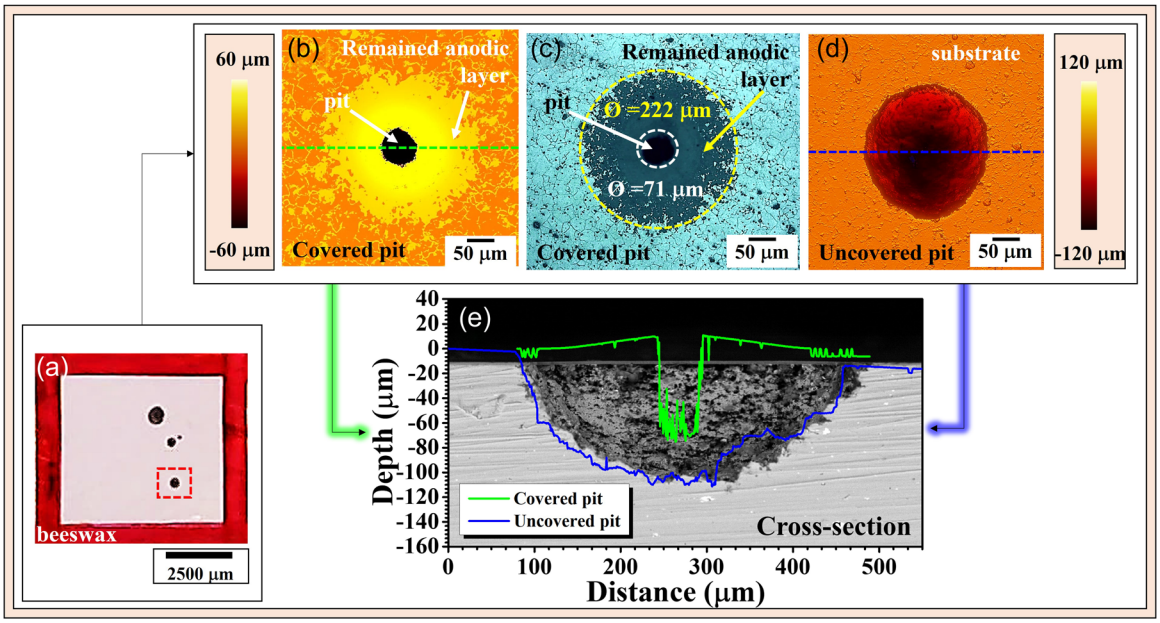

FIGURE 11 Micrographs corresponding to a pit in the AA7475 anodized aluminum alloy after anodic polarization test in 0.1 mol L^{-1} NaCl solution: (a) surface macrography (corresponding to polarization curve 2 shown in Figure 3); (b) optical profilometry image of the dashed squared region shown in (a); (c) optical microscope image corresponding to (b); (d) optical profilometry image of the substrate region shown in (b, c) after the removal of the corrosion products and the anodic layer; and (e) scanning electron micrograph of the cross-section of the region indicated by dashed lines shown in (b) and (d) and their depth profile. The red and yellow circles in (c) indicate the mouth of the pit in the anodic layer (before desmutting) and the real mouth of the pit after corrosion products and anodic layer removal, respectively. [Color figure can be viewed at wileyonlinelibrary.com]

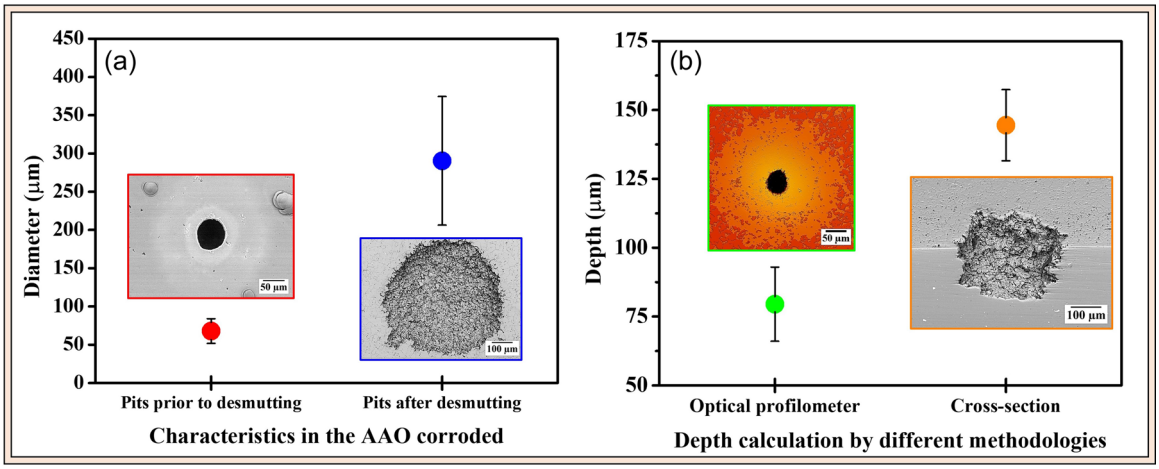

FIGURE 12 Statistical analysis of the pits formed in the AA7475 anodized aluminum alloy after anodic polarization test in 0.1 mol L^{-1} NaCl solution before and after desmutting: (a) comparison of the average diameter of the pits and (b) comparison of the depth calculation of the pits by different methodologies (optical profilometry and cross-sectional analysis). Each analysis was carried out by calculating 14 pits. [Color figure can be viewed at wileyonlinelibrary.com]

However, NSOM is a relatively new technique, and few studies have already been carried out to measure corrosion propagation; in the case of pits in anodized Al alloys, no work has so far been reported.

The use of characterization techniques that scrutinize the dimensions of areas affected by corrosion based on the responses arising from the metal below the corrosion products or alternative techniques to correctly assess the depth and width of the pit without the removal of the anodic and corrosion products layer would be of great help. In this sense, some research[86–88] have developed in situ methods to estimate the depth of pits during electrochemical experiments using a time series of surface micrographs. Faraday's law was employed in conjunction with this information. In these works, it was possible to obtain three-dimensional information with spatial coordinates using two-dimensional data from micrographs together with three-dimensional non-localized data from electrochemical measurements to estimate pit depths in steels. For anodized Al alloys, there is still no literature available. Furthermore, due to the transient nature of corrosion products, investigation of pit depth cannot be done using only electrochemical methods.[89,90] Therefore, up to date, cross-section analysis is apparently a proper method to assess the areas affected by corrosion.

Another point that must be taken into account is that initiation of pitting in anodized alloys occurs in the defects of the anodic layer due to dissolution associated with micrometer IMPs during anodizing process.[41,42,58,75] Currently, Takahashi et al.,[13,14] Zuo et al.,[15] and Ren and Zuo[16] focused their studies on pure Al, while only the works of Moutarlier et al.[17] and Ma et al.[41] reported findings from commercial alloys.

4 | CONCLUSIONS

(a) The methodology adopted in this study provides an accurate characterization of pitting in anodized aluminum alloys.
(b) Severe pitting attack under an anodic layer occurs in anodized AA7475 Al–Zn–Mg–Cu alloy due to highly occluded conditions that restrict mass transport between the interior of the pit and the bulk electrolyte, resulting in acidification at the corrosion front.
(c) The extent of the attacked areas by pitting is usually significantly greater than that estimated by techniques whose analysis is carried out only from the top surface.

AUTHOR CONTRIBUTIONS

João Victor de Sousa Araujo: Investigation; visualization; writing—original draft. **Mariana Xavier Milagre**: Review and editing. **Xiaorong Zhou**: Writing—review and editing. **Isolda Costa**: Project administration; supervision; writing—review and editing.

ACKNOWLEDGMENTS

The authors acknowledge Conselho Nacional de Desenvolvimento Científico e Tecnológico (CNPq) (406871/2021-3) and Fundação de Amparo à Pesquisa do Estado de São Paulo (FAPESP) (Proc. 2019/18388-1 and 2022/06935-0) for the Ph.D. grants of João Victor de Sousa Araujo.

CONFLICT OF INTEREST STATEMENT

The authors declare no conflict of interest.

DATA AVAILABILITY STATEMENT

Research data are not shared.

ORCID

João Victor de Sousa Araujo http://orcid.org/0000-0001-6375-0480
Mariana Xavier Milagre http://orcid.org/0000-0003-2048-2863
Xiaorong Zhou http://orcid.org/0000-0001-9943-3997
Isolda Costa http://orcid.org/0000-0002-4987-3334

REFERENCES

[1] J. Araujo, R. Pereira, R. Klumpp, I. Costa, *Quim. Nova* **2021**, *44*, 999.
[2] M. Schneider, W. Fürbeth, *Mater. Corros.* **2022**, *73*, 1752.
[3] G. E. Thompson, P. Skeldon, X. Zhou, K. Shimizu, H. Habazaki, C. J. E. Smith, *Aircr. Eng. Aerosp. Technol.* **2003**, *75*, 372.
[4] G. E. Thompson, H. Habazaki, K. Shimizu, M. Sakairi, P. Skeldon, X. Zhou, G. C. Wood, *Aircr. Eng. Aerosp. Technol.* **1999**, *71*, 228.
[5] J. V. de, S. Araujo, M. Milagre, I. Costa, *Crit. Rev. Solid State Mater. Sci.* **2023**, 1.
[6] J. M. Runge, *The Metallurgy of Anodizing Aluminum*, Springer International Publishing, Cham **2018**.
[7] M. Baumgärtner, H. Kaesche, *Corros. Sci.* **1990**, *31*, 231.
[8] M. Baumgärtner, H. Kaesche, *Mater. Corros.* **1991**, *42*, 158.
[9] M. Baumgärtner, H. Kaesche, *Mater. Corros.* **1988**, *39*, 129.
[10] H. Kaesche, *Mater. Corros.* **1988**, *39*, 153.
[11] H. Kaesche, in *Corrosion of Metals, Engineering Materials and Processes* (Ed: B. Derb), Springer, Berlin, Heidelberg **2003**, p. 324.
[12] N. Murer, R. G. Buchheit, *Corros. Sci.* **2013**, *69*, 139.
[13] H. Takahashi, K. Fujiwara, M. Seo, *Corros. Sci.* **1994**, *36*, 689.
[14] H. Takahashi, K. Kasahara, K. Fujiwara, M. Seo, *Corros. Sci.* **1994**, *36*, 677.
[15] Y. Zuo, P. H. Zhao, J. M. Zhao, *Surf. Coat. Technol.* **2003**, *166*, 237.
[16] J. Ren, Y. Zuo, *Surf. Coat. Technol.* **2005**, *191*, 311.
[17] V. Moutarlier, M. P. Gigandet, J. Pagetti, *Appl. Surf. Sci.* **2003**, *206*, 237.
[18] U. Donatus, M. Oluwatosin Bodunrin, A. Olayinka, M. Xavier Milagre, O. Rasaq Oloyede, S. Aribo, J. Victor de Sousa Araujo, C. de Souza Carvalho Machado, I. Costa (Ed: L. A. Dobrzański), in *Advanced Aluminium Composites and Alloys*, IntechOpen, **2021**.
[19] J. V. de Sousa Araujo, A. F. Santos Bugarin, U. Donatus, C. S. C. Machado, F. M. Queiroz, M. Terada, A. Astarita, I. Costa, *Corros. Eng. Sci. Technol.* **2019**, *54*, 575.
[20] C. de Souza Carvalho Machado, U. Donatus, M. X. Milagre, N. V. V. Mogili, R. A. R. Giorjão, R. E. Klumpp, J. Victor de S. Araujo, R. O. Ferreira, I. Costa, *Corrosion* **2019**, *75*, 628.
[21] Z. Wang, P. Zhang, X. Zhao, S. Rao, *Coatings* **2022**, *12*, 1899.
[22] G. N. Frantziskonis, L. B. Simon, J. Woo, T. E. Matikas, *Eur. J. Mech. A* **2000**, *19*, 309.
[23] M. G. Koul, *Corrosion* **2003**, *59*, 563.
[24] R. J. K. Wood, *Proc. Inst. Mech. Eng. C* **1990**, *204*, 63.
[25] M. K. Cavanaugh, R. G. Buchheit, N. Birbilis, *Eng. Fract. Mech.* **2009**, *76*, 641.
[26] E. Schmidl, R. Pippig, R. Morgenstern, T. Lampke, I. Scharf, *Corros. Eng. Sci. Technol.* **2018**, *53*, 194.
[27] I.-W. Huang, B. L. Hurley, F. Yang, R. G. Buchheit, *Electrochim. Acta* **2016**, *199*, 242.
[28] B. G. Prakashaiah, D. Vinaya Kumara, A. Anup Pandith, A. Nityananda Shetty, B. E. Amitha Rani, *Corros. Sci.* **2018**, *136*, 326.
[29] R. del Olmo, E. López, E. Matykina, U. Tiringer, J. M. C. Mol, M. Mohedano, R. Arrabal, *Prog. Org. Coat.* **2023**, *182*, 107667.
[30] K. Shimizu, G. M. Brown, K. Kobayashi, P. Skeldon, G. E. Thompson, G. C. Wood, *Corros. Sci.* **1998**, *40*, 1049.
[31] E. Cor, *Annu. B. ASTM Stand.* **1999**, *94*, 1.
[32] N. Alr, D. Lakehurst, *US Patent MIL-A-8625F*, 1993.
[33] E. Kock, M. Beneke, C. Gerlach, *US Patent CA2491095A10*, 2004.
[34] ALCOA 7475, *High Strength, Close Grain Iron Casting, Alloy Digest*, Aluminum Company of America, USA **1989**, *38*, Al.
[35] U. Donatus, J. V. de Sousa Araujo, C. de Souza Carvalho Machado, N. V. Vardhan Mogili, R. A. Antunes, I. Costa, *Corros. Eng. Sci. Technol.* **2019**, *54*, 205.
[36] G. M. Scamans, M. F. Frolish, W. M. Rainforth, Z. Zhou, Y. Liu, X. Zhou, G. E. Thompson, *Surf. Interface Anal.* **2010**, *42*, 175.
[37] A. Afseth, J. H. Nordlien, G. M. Scamans, K. Nisancioglu, *Corros. Sci.* **2001**, *43*, 2093.
[38] J. Wang, X. Zhou, G. E. Thompson, J. A. Hunter, Y. Yuan, *Mater. Charact.* **2015**, *99*, 109.
[39] J. Wang, X. Zhou, G. E. Thompson, J. A. Hunter, Y. Yuan, *Metall. Mater. Trans. A* **2016**, *47*, 4268.
[40] M. Paz Martínez-Viademonte, S. T. Abrahami, T. Hack, M. Burchardt, H. Terryn, *Coatings* **2020**, *10*, 1106.
[41] Y. Ma, H. Wu, X. Zhou, K. Li, Y. Liao, Z. Liang, L. Liu, *Corros. Sci.* **2019**, *158*, 108110.
[42] J. V. de Sousa Araujo, M. Xavier Milagre, R. Emil Klumpp, V. Hugo Ayusso, U. Donatus, I. Costa, *Corros. Eng. Sci. Technol.* **2022**, *57*, 380.
[43] E. Kock, C. Gerlach, M. Beneke, *Germany Patent DE10361888B30*, 2004.
[44] Anon, Standard Practice for Preparing, Cleaning, and Evaluating Corrosion Test Specimens, *ASTM Spec. Tech. Publ.* **1985**, 505.
[45] M. Curioni, M. Saenz De Miera, P. Skeldon, G. E. Thompson, J. Ferguson, *J. Electrochem. Soc.* **2008**, *155*, C387.
[46] F. Andreatta, H. Terryn, J. H. W. de Wit, *Electrochim. Acta* **2004**, *49*, 2851.
[47] C. P. de Abreu, I. Costa, H. G. de Melo, N. Pébère, B. Tribollet, V. Vivier, *J. Electrochem. Soc.* **2017**, *164*, C735.
[48] A. F. S. Bugarin, C. P. De Abreu, M. Terada, H. G. De Melo, I. Costa, *Mater. Today Commun.* **2020**, *25*, 101591.
[49] S.-S. Wang, G. S. Frankel, J.-T. Jiang, J.-F. Chen, S.-L. Dai, L. Zhen, *J. Electrochem. Soc.* **2013**, *160*, C493.
[50] N. Birbilis, M. K. Cavanaugh, R. G. Buchheit, *Corros. Sci.* **2006**, *48*, 4202.
[51] Y. Ma, X. Zhou, G. E. Thompson, T. Hashimoto, P. Thomson, M. Fowles, *Mater. Chem. Phys.* **2011**, *126*, 46.
[52] F. Mazzolani, *Aluminium Alloy Structures*, 2nd ed., CRC Press, Boca Raton, FL **2014**.
[53] Q. Meng, G. S. Frankel, *J. Electrochem. Soc.* **2004**, *151*, B271.
[54] J. V. de Sousa Araujo, M. X. Milagre, R. O. Ferreira, C. de Souza Carvalho Machado, C. P. de Abreu, I. Costa, *Metallogr.Microstruct. Anal.* **2020**, *9*, 744.
[55] Y. Ji, Y. Xu, B. Zhang, Y. Behnamian, D. Xia, W. Hu, *Trans. Nonferrous Met. Soc. China* **2021**, *31*, 3205.

[56] Y. Ma, X. Zhou, G. E. Thompson, M. Curioni, X. Zhong, E. Koroleva, P. Skeldon, P. Thomson, M. Fowles, *Corros. Sci.* **2011**, *53*, 41.
[57] M. Saenz De Miera, M. Curioni, P. Skeldon, G. E. Thompson, *Surf. Interface Anal.* **2010**, *42*, 241.
[58] J. V. Araujo, M. Xavier Milagre, A. D Gabbardo, R. E. Klumpp, I. Costa, *ECS Meet. Abstr.* **2022**, *MA2022-02*, 2475.
[59] M. Warmuzek, in *Metallography and Microstructures*, ASM International, **2004**, pp. 711.
[60] J. M. Runge, in *15th Annu. Anodizing Conf. and Expo, the Aluminum Anodisers Council*, Trace Elements **2013**, 1.
[61] G. Scampone, G. Timelli, *Adv. Eng. Mater.* **2022**, *24*, 2101480.
[62] Y. Ma, X. Zhou, J. Wang, G. E. Thompson, W. Huang, J. O. Nilsson, M. Gustavsson, A. Crispin, *J. Electrochem. Soc.* **2014**, *161*, C312.
[63] Y. Ma, X. Zhou, G. E. Thompson, J.-O. Nilsson, M. Gustavsson, A. Crispin, *Surf. Interface Anal.* **2013**, *45*, 1479.
[64] R. Haynes, *Optical Microscopy of Materials*, Springer, Boston, MA **1984**.
[65] A. Ul-Hamid, *A Beginners' Guide to Scanning Electron Microscopy*, Springer International Publishing, Cham **2018**.
[66] K. Shimizu, T. Mitani, *New Horizons of Applied Scanning Electron Microscopy*, 45 Springer, Berlin, Heidelberg **2010**.
[67] E. McCafferty, *Corros. Sci.* **1995**, *37*, 481.
[68] G. S. Frankel, *Corrosion* **1998**, *145*, 2186.
[69] M. A. Amin, S. S. Abd El Rehim, A. S. El-Lithy, *Corros. Sci.* **2010**, *52*, 309.
[70] Z. Szklarska-Smialowska, *Corros. Sci.* **1999**, *41*, 1743.
[71] A. Muñoz, J. B. Bessone, *Corros. Sci.* **1999**, *41*, 1447.
[72] J. I. Goldstein, D. E. Newbury, P. Echlin, D. C. Joy, C. E. Lyman, E. Lifshin, L. Sawyer, J. R. Michael, *Scanning Electron Microscopy and X-Ray Microanalysis*, Springer, Boston, MA **2003**.
[73] T. J. Shaffner, R. D. V. Veld, *J. Phys. E.* **1971**, *4*, 633.
[74] Y. Ma, X. Zhou, K. Li, S. Pawar, Y. Liao, Z. Jin, Z. Wang, H. Wu, Z. Liang, L. Liu, *J. Electrochem. Soc.* **2019**, *166*, C296.
[75] H. Wu, Y. Ma, W. Huang, X. Zhou, K. Li, Y. Liao, Z. Wang, Z. Liang, L. Liu, *J. Electrochem. Soc.* **2018**, *165*, 573.
[76] R. K. Mishra, A. K. Zachariah, S. Thomas, in *Microscopy Methods in Nanomaterials Characterization* (Eds: S. Thomas, R. Thomas, A. K. Zachariah, R. K. Mishra), Elsevier, Amsterdam **2017**, pp. 383.
[77] T. Gandhi, *Microelectronics Failure Analysis*, ASM International, Materials Park, OH **2019**.
[78] X. Zhou, G. E. Thompson, G. M. Scamans, *Corros. Sci.* **2003**, *45*, 1767.
[79] B. Liu, X. Zhou, X. Zhang, *Trans. Nonferrous Met. Soc. China* **2020**, *30*, 56.
[80] Z. Shi, H. Zeng, Z. Zhang, X. Zhang, L. Ćurković, V. Mandić, S. Fu, W. Wang, J. Liu, L. Zhao, X. Zhang, *J. Magn. Magn. Mater.* **2023**, *565*, 170222.
[81] H.-J. Chen, Y.-C. Chen, P.-C. Lin, K. Lin, J. C. Lin, M.-J. Chen, H.-C. Lin, *Materials* **2023**, *16*, 6149.
[82] N. Gong, H. Seet, J. Cao, T. Luai Meng, Y. Wang, D. C. C. Tan, C. Kiang Ivan Tan, A. Suwardi, Q. Zhu, D. J. Blackwood, M. Ling Sharon Nai, H. Liu, *Mater. Lett.* **2023**, *331*, 133434.
[83] R. M. Pidaparti, R. K. Patel, *Corros. Sci.* **2010**, *52*, 3150.
[84] R. M. Pidaparti, R. R. Patel, *J. Mater. Eng. Perform.* **2011**, *20*, 1114.
[85] M. Conroy, J. Armstrong, *J. Phys. Conf. Ser.* **2005**, *13*, 458.
[86] A. M. Zimer, E. C. Rios, L. H. Mascaro, E. C. Pereira, *Electrochem. Commun.* **2011**, *13*, 1484.
[87] A. M. Zimer, E. C. Rios, P. C. D. Mendes, W. N. Gonçalves, O. M. Bruno, E. C. Pereira, L. H. Mascaro, *Corros. Sci.* **2011**, *53*, 3193.
[88] A. M. Zimer, M. A. S. De Carra, E. C. Rios, E. C. Pereira, L. H. Mascaro, *Corros. Sci.* **2013**, *76*, 27.
[89] C. Liu, R. G. Kelly, *Corrosion* **2019**, *75*, 1285.
[90] Y. Wang, G. Cheng, *Mater. Des.* **2016**, *94*, 176.

How to cite this article: J. V. de Sousa Araujo, M. X. Milagre, X. Zhou, I. Costa, *Mater. Corros.* **2024**, *75*, 599–613. https://doi.org/10.1002/maco.202313977